Asymmetric anion effects of anions in ionic liquids: Crystal polymorphs and magnetic properties

Hiroshi Abe [a], Shin Kobayashi [b], Kohei Ogawa [b], Kanta Imai [b], Kaito Koshiji [b], Miku Hoshino [b], Takaaki Hirano [a], Yoshiaki Hata [c], Hiroaki Kishimura [a], Mikio Uruichi [d]

[a] Department of Materials Science and Engineering, National Defense Academy, Yokosuka 239-8686, Japan
[b] Yokosuka High School, 3-109 Kugo, Yokosuka 238-0022, Japan
[c] Department of Applied Physics, National Defense Academy, Yokosuka 239-8686, Japan
[d] Institute for Molecular Science, Myodaiji, Okazaki 444-8585, Japan

ARTICLE INFO

ABSTRACT

In this study, the phase transitions and magnetic properties of magnetic ionic liquids (mILs) were investigated at low temperatures. The mILs were $[C_n mim]_2[MnCl_{4-m}Br_m]$ (n = 2, 3, and 4; m = 0, 1, 2, 3, and 4), where $[C_n mim]^+$ is 1-alkyl-3-methylimidazolium. Here, simultaneous X-ray diffraction and differential scanning calorimetry were used to determine the crystal polymorphs in the mILs. The results showed that shorter alkyl chain lengths of cations and symmetric anions aided crystallization. Melting points in $[C_2 mim]_2[MnCl_{4-m}Br_m]$ were also found to be strongly dependent on asymmetric anionic configurational and cationic conformational entropies. Furthermore, the asymmetric anion effect contributed slightly to the paramagnetic properties of mILs.

1. Introduction

Ionic liquids (ILs) have been extensively researched and synthesized for various applications [1–7]. Combining cations and anions can broaden the range of the ILs' industrial applications [8–11]. For example, ILs have been widely used in electrochemical devices [12], catalysis [13], CO_2 capture [14], and cellulose dissolution [15] using their chemical, electrochemical, and thermal stabilities. However, there are difficulties in selecting the desired IL from numerous cation and anion combinations. Hence, the IL properties were predicted using a computer to optimize the task-specific ILs for each application [16–19].

Hayashi and Hamaguchi discovered a magnetic ionic liquid (mIL) [20] named 1-Butyl-3-methylimidazolium tetrachloroferrate $[C_4 mim][FeCl_4]$. $[C_4 mim][FeCl_4]$ was discovered to be paramagnetic using SQUID (superconducting quantum interference device) magnetometry. The formations of $[FeCl_4]^-$ and $[FeBr_4]^-$ anions were clarified by Raman spectroscopy and density functional theory (DFT) calculations [21–26]. In contrast to the paramagnetic $[C_4 mim][FeCl_4]$, the antiferromagnetic $[C_2 mim][FeCl_4]$ had a Neel temperature (T_N) of 4 K [27,28]. The unit cell's molecular orientational and positional orders were determined using single crystal X-ray structure analysis [28]. Besides, the magnetic ordering of deuterated-$[C_2 mim][FeCl_4]$ was directly determined by neutron diffraction [29]. Magnetic Bragg reflections were allowed for antiferromagnetic ordering along a and c axes. A magnetic phase transition from antiferromagnetic to ferrimagnetic ordering was observed in $[C_2 mim][FeCl_4]$ [30] under high pressure. Superex-

change pathways comprehended three-dimensional ordering. Diffraction methods and magnetic susceptibility measurements determined the crystal structure and antiferromagnetic properties of $[C_1 mim][FeBr_4]$ as another mIL type [31]. $[C_1 mim][FeBr_4]$ had a T_N of 7.7 K. Antiparallel ordering can be explained by the layered structure of $[FeBr_4]^-$. The magnetic properties of mILs involve the symmetric anions $[FeCl_4]^-$ and $[FeBr_4]^-$. The asymmetric anion effect of mILs was recently reported [32]. The phase behavior related to the magnetic properties of $[C_4 mim][FeCl_{4-m}Br_m]$ (m = 0, 1, 2, 3, and 4) were observed using simultaneous X-ray diffraction (XRD) and differential scanning calorimetry (DSC). The entropic effect was also discussed using the DFT calculations.

In this study, the presence of symmetric and asymmetric anions in the mILs was investigated by Raman spectroscopy, SQUID, and simultaneous XRD and DSC measurements. The formations of Br-substituted asymmetric anions in $[C_n mim]_2[MnCl_{4-m}Br_m]$ was revealed by Raman spectra. The cationic conformers and the presence of symmetric and asymmetric anions had a considerable influence on the phase behaviors of $[C_n mim]_2[MnCl_{4-m}Br_m]$ at low temperatures. Furthermore, the mILs exhibited paramagnetic behavior and estimating the effective paramagnetic moment (μ_{eff}) of mILs demonstrated insignificant n and m dependences on it.

2. Materials and methods

The mILs with the presence of symmetric and asymmetric anions were produced by mixing the hydrophilic ILs, $MnCl_2 \cdot 4H_2O$ (Sigma-Aldrich Co.), and $MnBr_2 \cdot 4H_2O$ (Mitsuwa Chemicals Co.). The ILs were [C_2mim][Cl], [C_3mim][Cl], [C_3mim][Br], and [C_4mim][Br] (IoLiTec Co.); [C_2mim][Br] (Kanto Chemical Co.); [C_4mim][Cl] (Acros Organics Co.). [$C_n$mim]$_2$[$MnCl_{4-m}Br_m$] (n = 2, 3, and 4; m = 0, 1, 2, 3, and 4) were synthesized spontaneously in a dry box with helium gas flowing to reduce atmospheric H_2O. After mixing in the dry box, the residual water in the mixtures was evaporated for a week by vacuum drying at room temperature. According to DFT calculations [33] and experiments [34], the [C_2mim]$^+$, [C_3mim]$^+$, and [C_4mim]$^+$ cations, respectively, have two, three, and four observable conformers (Fig. 1). The stable conformers of [C_2mim]$^+$ are *planar* (p) and *nonplanar* (n). While, nt, ng, and ng' represent stable [C_3mim]$^+$ conformers, t, g, and g' represent *trans*, *gauche*, and *gauche'*, respectively. [C_4mim]$^+$ is a well-known conformational polymorph that is expressed by ntt, ngt, ng't, and ng'g' [33]. In intramolecular geometry, conformational degrees of freedom contribute to conformational entropy, S_{confor} [19].

Raman spectra were measured using Via Reflex (RENISHAW). With a power of 0.35 mW, a 785 nm semiconductor laser was used as an excitation source. The Raman bands of Mn-containing samples became the most intense in the previous study [35] when the 785 nm excitation was used. Using the 532 nm Raman excitation light, the phase changes were not observed due to the fluorescence background.

A vertical goniometer was used to perform conventional powder XRD at room temperature (SmartLab; Rigaku Co.). The incident X-ray wavelength was Cu Kα (λ = 1.542 Å). A 1D detector (D/teX Ultra 250; Rigaku Co.) with a fluorescent X-ray reduction mode reduced the Mn fluorescent X-ray. Since the 1D detector possesses high energy resolution, the fluorescence background can be reduced by changing a window of pulse height. The background using the reduction mode decreased by less than 10% of the same for the normal mode. Since [C_2mim]$_2$[$MnCl_{4-m}Br_m$] and [C_3mim]$_2$[$MnBr_4$] were crystal states at room temperature, powder diffraction patterns were collected using the sample rotation stage at room temperature to remove the preferred orientation of the Debye rings. The cell encased the sample rotation stage, through which dry helium gas flowed to reduce air scattering and remove atmospheric moisture. *FOX* [36] and *Conograph* [37] were used to analyze the crystal structures. *Conograph* was used to calculate the possible lattice parameters and space groups, and *FOX* was used to identify the space group through global optimization.
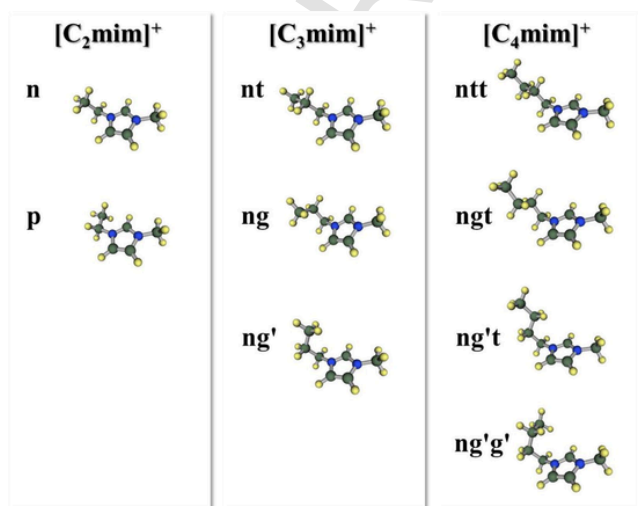

Fig. 1. Optimized molecular structures of [$C_n$mim]$^+$ by density functional theory (DFT) calculations. p, n, t, g, and g' denote *planar*, *nonplanar*, *trans*, *gauche*, and *gauche'*, respectively.

Complex phase changes can be differentiated using simultaneous XRD and DSC measurements. The D/teX Ultra 250 was integrated for rapid scanning, and dry nitrogen gas flowed through the DSC attachment. The temperature of the simultaneous measurements ranged between 173 K and 323 K, with cooling and heating rates of 5 K/min.

The DSC measurements at high temperatures only for [C_2mim]$_2$[$MnCl_{4-m}Br_m$] were performed using high-sensitivity DSC (DSC7000X, Hitachi High-Tech Co.) at a cooling/heating rate of 5 K/min. The temperature was 200–420 K.

Magnetic properties were measured in a 100 Oe magnetic field using a SQUID magnetometer (MPMS-XL; Quantum Design). The measurements were conducted over temperatures of 2–300 K. Cooling and heating rates ranged from 1 to 10 K/min.

The optimized molecular structures of anions were evaluated using *Firefly* (*PC GAMESS*) [38,39]. The B3LYP calculation used the 6–31G(d) basis set and a Mn^{2+} atom with S = 5/2 in the system. DFT also estimate the Raman bands.

3. Results and discussion

3.1. Raman bands of [$C_n$mim]$_2$[$MnCl_{4-m}Br_m$]

Fig. 2 shows the Raman spectra of [C_2mim]$_2$[$MnCl_{4-m}Br_m$] (m = 0, 1, 2, 3 and 4) at room temperature (296 K). The calculated Raman bands are represented by the vertical bars in the DFT calculations (Fig. 2). The Raman band of [C_2mim]$_2$[$MnCl_4$] at 260 cm^{-1} was identified as the Mn–Cl vibrational mode. The Raman spectrum of [C_2mim]$_2$[$MnCl_4$] in Fig. 2 was comparable to that of hybrid compounds containing (Quinuclidinium)[$MnCl_4$] [40]. Conversely, the Mn–Br stretching mode of [C_2mim]$_2$[$MnBr_4$] appeared at 160 cm^{-1} in (Fig. 2). It was found that [$MnCl_4$]$^{2-}$ and [$MnBr_4$]$^{2-}$ are created in the mILs. In an earlier study [32], DFT was used to optimize [$FeCl_4$]$^-$ and [$FeBr_4$]$^-$, and the Raman bands at 333 cm^{-1} and 205 cm^{-1} were delegated as Fe–Cl and Fe–Br stretching vibrations, respectively. The intra-atomic distances between Fe and Br grew longer when compared to the Fe–Cl distance [32]. In the Raman spectra, both symmetric Fe- and Mn-based anions displayed the same tendency.

The next step is to distinguish the asymmetric anion effect from the symmetric one. Due to anion asymmetricity, the number of orientational relationships between cation and anion alters geometrically [32]. Configurational entropy or S_{config} is defined as intermolecular geometry [19]. Structural entropy, $\Delta_{str}S$, is provided as follows [19]:

$$\Delta_{str}S = \Delta_{confor}S + \Delta_{config}S \tag{1}$$

Asymmetric [$MnCl_{4-m}Br_m$]$^{2-}$ (m = 1, 2, and 3) was classified into two groups based on the cation–anion pairs [32]. The number of cases of the cation–anion pairs was four (Group S_4), and six (Group S_6) according to configurational entropy (S_{config}). [$MnCl_3Br$]$^{2-}$ and [$MnClBr_3$]$^{2-}$ are members of Group S_4, the point group of which is C_{3v}. In contrast, [$MnCl_2Br_2$]$^{2-}$ is assigned to S_6 (C_{2v}) group. Furthermore, asymmetric anions transform into distorted tetrahedrons because the Mn–Cl distance was shorter than the Mn – Br distance. At ~230 cm^{-1}, the band splitting of asymmetric [$FeCl_{4-m}Br_m$]$^-$ (m = 1, 2, and 3) was observed, with each band shifting to a lower wavenumber as the Br-substitution increased. Here, the asymmetric anions were responsible for the band splitting at ~180 cm^{-1} (Fig. 2). As the calculated Raman band shifted, the weak Raman band at 280 cm^{-1} shifted to a higher wavenumber with the increasing m. Consequently, the similarity between the calculated and observed Raman bands suggests that asymmetric [$MnCl_{4-m}Br_m$]$^{2-}$ existed before the formation of symmetric [$MnCl_4$]$^{2-}$ and [$MnBr_4$]$^{2-}$.

[C_3mim]$_2$[$MnCl_{4-m}Br_m$] and [C_4mim]$_2$[$MnCl_{4-m}Br_m$] Raman bands are presented in Figs. S1 and S2, respectively. The anions' Br substitution effect was also observed in both systems. Therefore, the formation
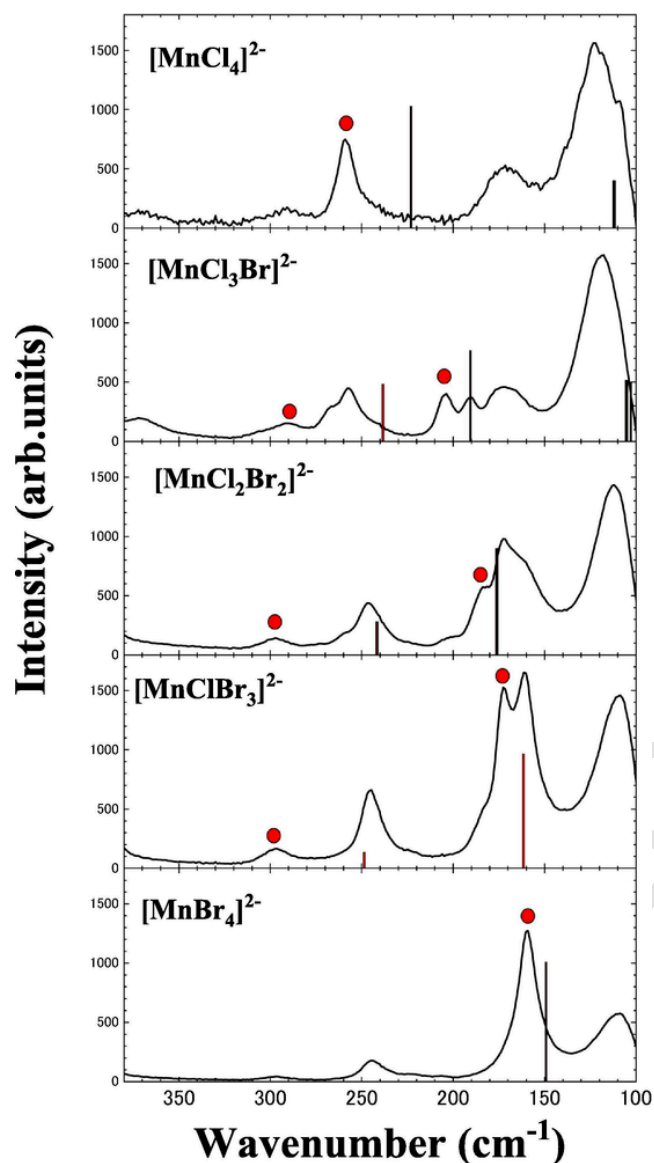
Fig. 2. Raman spectra of $[C_2mim]_2[MnCl_{4-m}Br_m]$. The vertical bars show the evaluated Raman bands.

of $[MnCl_{4-m}Br_m]^{2-}$ was not hindered because of the cation alkyl chain length.

3.2. Crystal structures of magnetic ionic liquids

The crystal structure of $[C_1mim][FeBr_4]$ was determined previously [31], and the space group was discovered to be $P2_1$. The density (ρ) was calculated to be 2.395 g/cm³. When compared to conventional ILs, the densities of the mILs were found to be higher. At room temperature, $[C_2mim]_2[MnCl_{4-m}Br_m]$ and $[C_3mim]_2[MnBr_4]$ were crystallized. Consequently, the crystal structures of the aforementioned mILs were determined at room temperature using conventional powder diffraction with a sample rotation stage. Molecular orientational and positional orders in the unit cell are important in interpreting the crystal polymorph. Furthermore, the cationic conformers aided in the formation of crystal polymorphs at low temperatures [41–46] and high pressures [47–51].

Fig. 3 depicts XRD patterns of $[C_2mim]_2[MnCl_{4-m}Br_m]$ at room temperature. The Bragg reflection represents the long lattice constants at low scattering angles. XRD pattern of $[C_2mim]_2[MnClBr_3]$ was similar to that of $[C_2mim]_2[MnBr_4]$. Crystallographic parameters were ob-

tained through structure analysis (Table 1). The calculated densities increased proportionally to the Br substitutions, while the β angles decreased. $[C_2mim]_2[MnCl_4]$ was discovered to be $C2$ (Table 1). However, the crystal structure of $[C_2mim]_2[MnBr_4]$ was determined to be $P2_1$ with a smaller unit cell than $[C_2mim]_2[MnCl_4]$. Despite the symmetric anions, each crystal structure was unique. This means halogen types considerably altered the molecular interaction between cation and anion. Furthermore, from the space groups of $[C_2mim]_2[MnCl_{4-m}Br_m]$ (Table 1), the crystal structures were divided into two groups: (i) $m = 0, 1$, and 2 have non-screw symmetry, and (ii) $m = 3$ and 4 possess screw symmetry. The crystal structures of the mILs were unaffected by a single substitution for the anions. In contrast, the crystal structure of $[C_2mim]_2[MnCl_2Br_2]$ did not coincide with the crystal groups of $[C_2mim]_2[MnCl_4]$ and $[C_2mim]_2[MnBr_4]$ (Table 1). $[MnCl_2Br_2]^{2-}$ causes entirely different molecular interactions between the cation and anion in the crystal state in asymmetric anions. Therefore, $[MnCl_2Br_2]^{2-}$ is considered a novel type of an anion.

The atomic scattering factor for X-ray depends on the number of electrons (the atomic number). Therefore, heavy atoms such as [17]Cl, [25]Mn and [35]Br are enhanced, although cations containing light atoms such as [6]C, ^{1}H, and [7]N are X-ray insensitive. Cationic conformations were not thoroughly determined. Fig. S3 depicts networks of tetrahedral anion in the unit cells of $[C_2mim][MnCl_{4-m}Br_m]$. The tetrahedral orientational disorders explain large lattice constants. In the crystal state, the substituted Br of $[MnCl_3Br]^{2-}$ had no orientational order. Note that the two-dimensional ordering of $[MnCl_{4-m}Br_m]^{2-}$ did not occur in the unit cells (Fig. S3). This means that the $[C_2mim]_2[[MnCl_{4-m}Br_m]$ system cannot support intraplane interactions like $[C_1mmim][FeBr_4]$ [31].

At room temperature, $[C_3mim]_2[MnBr_4]$ was in a crystal state. Fig. S4 depicts the observed and calculated XRD patterns. The crystal structure that was determined is shown in Table 1. $[C_3mim]_2[MnBr_4]$ has larger lattice constants and a lower density than $[C_2mim]_2[MnBr_4]$ (Table 1). The alkyl chain length can tune the intermolecular distances among the $[MnCl_{4-m}Br_m]^{2-}$ anions.

3.3. X-ray diffraction and differential scanning calorimetry (DSC) of $[C_3mim]_2[MnBr_4]$

Despite the symmetric anion, complicated and irreversible phase behavior of $[C_3mim]_2[MnBr_4]$ was observed at low temperatures using simultaneous XRD diffraction and DSC measurements (Fig. 4). Following cooling and heating, entirely distinct crystal polymorphs emerged. In terms of cooling, crystallization occurred at 307 K (T_{C1}), accompanied by new Bragg reflections and an exothermal peak. This crystal is known as the α phase. The XRD pattern in Fig. 4 differs from that obtained at 296 K (Fig. S4), and it was obtained using the sample rotation stage to minimize the preferred orientation. Because of the high atomic scattering factor for X-rays, only Mn and Br atoms were enhanced in Cu Kα radiation. The anion – anion correlation produced strong Bragg reflections. At 288 K (T_{C2}), a crystal-crystal (α-β) phase transition was observed after further cooling. Furthermore, weak Bragg reflections, represented by green open circles in Fig. 4, appeared during the β phase. Cooling at 225 K induced another crystal-crystal (β-γ) phase transition (T_{C3}). Besides, new Bragg reflections differentiate the γ phase (the blue open circles in Fig. 4). The crystal polymorph of the α- β-γ phases upon cooling implies that anions' simple Br substitution enforces a phase variety.

Fig. 4 shows the irreversible crystal polymorph after heating. Firstly, the endothermal peak was observed with additional Bragg reflections at 251 K (T_{C4}). The new phase is called the δ phase. Since strong Bragg reflections above and below T_{C4} were nearly identical, the Br positional and orientational orders did not change at T_{C4}. Despite the heating process, a low-symmetry crystal with an endothermal peak appeared at T_{C4}. This result contradicts the expected phase transition.
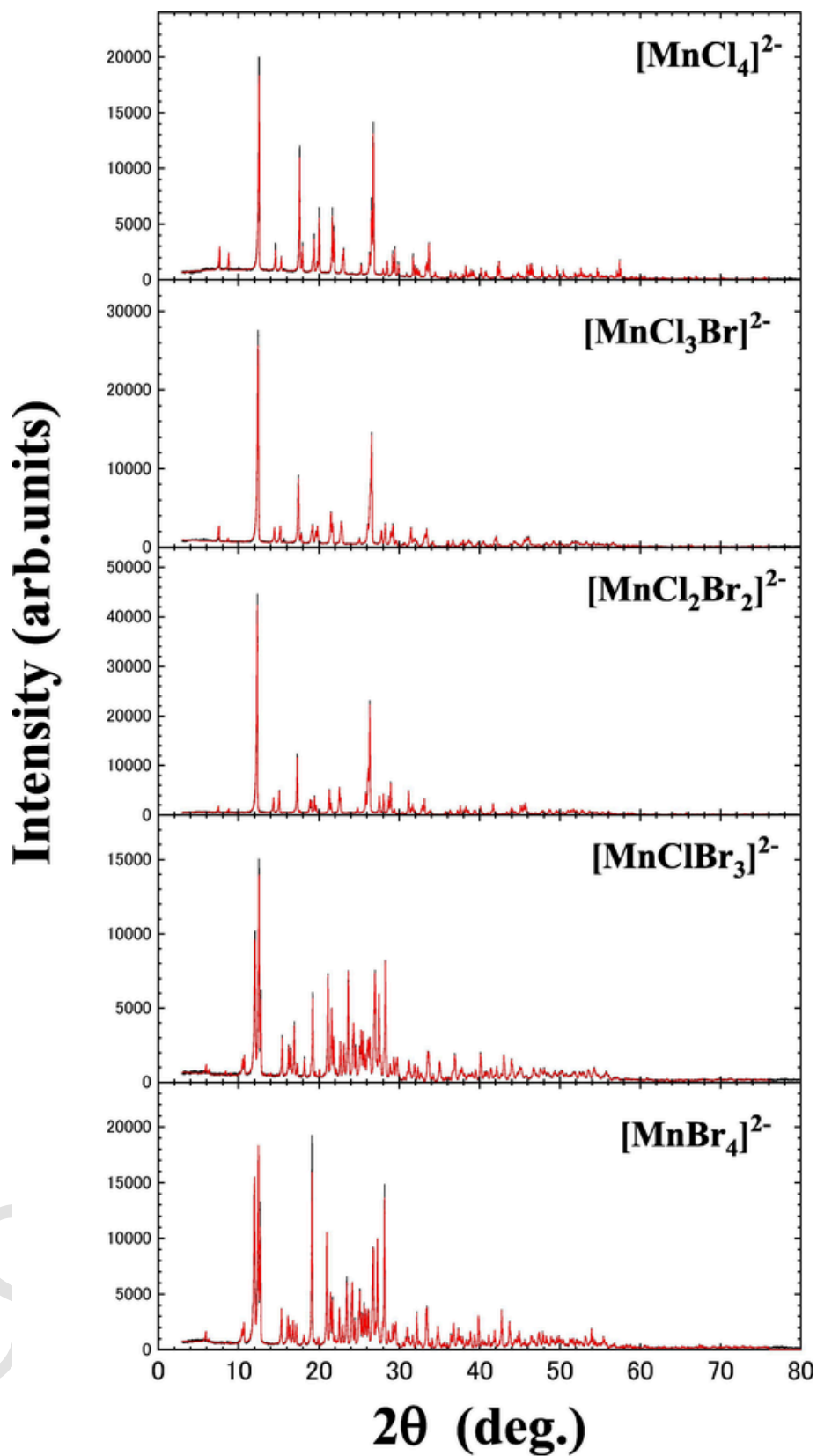
Fig. 3. X-ray diffraction patterns at room temperature of [C$_2$mim]$_2$[MnCl$_{4-m}$Br$_4$] and [C$_3$mim]$_2$[MnBr$_4$].

Secondly, at 266 K (T_{C5}), a drastic phase transition (δ-ε phase transition) was observed with the disappearance of the strong Bragg reflections (Fig. 4). The absence of strong Bragg reflections indicated that the anion orientations became disordered in the unit cell. The ε phase

Table 1
Crystallographic data for $[C_2mim]_2[MnCl_{4-m}Br_4]$ and $[C_3mim]_2[MnBr_4]$.

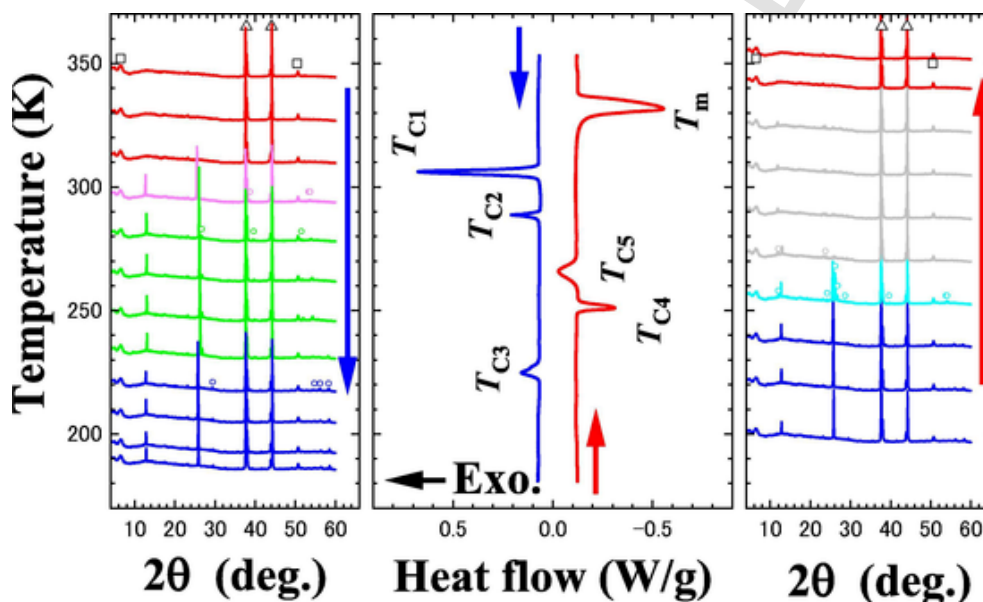| m	Space group	a (nm)	b (nm)	c (nm)	α (°)	β (°)	γ (°)	Z	ρ (g/cm³)	R (%)	R_w (%)
0	C2	1.9754	2.0136	1.4103	90	134.37	90	12	2.082	10.6	11.6
1	C2	1.9904	2.0284	1.4203	90	134.43	90	12	2.255	7.9	12.1
2	C2	2.4752	1.4479	1.4489	90	125.80	90	12	2.403	6.0	10.0
3	P2₁	1.3872	1.0240	1.4749	90	94.142	90	6	2.633	6.6	8.4
4	P2₁	1.3937	1.0300	1.4839	90	94.342	90	6	2.799	9.0	9.1

Fig. 4. X-ray diffraction and DSC of $[C_3mim]_2[MnBr_4]$.

was characterized by only a cationic order. Finally, at 332 K (T_m), the ε phase melted. It is emphasized here that the crystal polymorphs of $[C_3mim]_2[MnBr_4]$ are highly unusual. This is because, in the conventional ILs, some phases during heating coincided with those during cooling at low temperatures [41–45].

3.4. Differential scanning calorimetry (DSC) thermal traces of $[C_nmim]_2[MnCl_{4-m}Br_m]$

DSC detected low-temperature phase transitions of $[C_2mim]_2[MnCl_{4-m}Br_m]$ (Fig. 5). $[C_2mim]_2[MnCl_4]$ showed simple crystallization (T_C = 314 K) and melting (T_m = 355 K). Despite the simple molecular system, hysteresis was significant. The high T_m indicates a strong molecular interaction between the cation and anion. One Br was substituted to clarify the asymmetric anion effect of the anions. Cooling in $[C_2mim]_2[MnCl_3Br]$ induced the crystal polymorph. The distinct exothermal peaks determined T_{C1} (316 K), T_{C2} (301 K), and T_{C3} (297 K) (Fig. 5). $[C_2mim]_2[MnCl_3Br]$ melted at 343 K (T_m), which was less than the T_m of $[C_2mim]_2[MnCl_4]$. Conversely, $[C_2mim]_2[MnCl_2Br_2]$ phase transitions were represented by simple crystallization upon cooling and crystal polymorph upon heating. Furthermore, the T_m of $[C_2mim]_2[MnCl_2Br_2]$ was reduced by two Br substitutions. A similar phase behavior was obtained in the m = 3 and m = 4 system, (Fig. 5). Although the phase transition temperatures differed, simple crystallization (T_{C1}) upon cooling, crystallization (T_{C2}), and melting (T_m) upon heating were all classified as the same group of phase transitions. T_m of $[C_2mim]_2[MnCl_{4-m}Br_m]$ was found to be dependent on the configurational entropy, $\Delta_{config}S$, of the asymmetric anions. $\Delta_{config}S$ of Group S_4 and Group S_6 are 11.5 and 14.9 [J/(K·mol)], respectively. The largest $\Delta_{config}S$ of Group S_6 explained the lowest T_m of $[C_2mim]_2[MnCl_2Br_2]$. To

calculate the absolute entropy (S), we must first calculate the kinetic entropy, $\Delta_{kin}S$ [19]. Fusion entropy, $\Delta_{fus}S$, is given as follows [19]:

$$\Delta_{fus}S = \Delta_{kin}S + \Delta_{str}S \tag{2}$$

However, in this study, the melting points are qualitatively estimated only by $\Delta_{str}S$ in Eq. (1).

Using XRD and DSC simultaneously, the phase behavior of $[C_3mim]_2[MnCl_{4-m}Br_m]$ was investigated to clarify the alkyl chain length effect of cations. The crystallization was caused by symmetric $[MnCl_4]^{2-}$ upon cooling and melting upon heating (Fig. 6). When $[C_3mim]_2[MnCl_3Br]$ was cooled, it did not crystallize (Fig. 6). Glass transition (T_g = 222 K) and cold crystallization (T_{CC} = 259 K) followed heating. Moreover, the glass transition upon cooling and cold crystallization upon heating of $[C_3mim]_2[MnCl_2Br_2]$ were observed. The glass transitions of $[C_3mim]_2[MnCl_3Br]$ and $[C_3mim]_2[MnCl_2Br_2]$ are derived from the larger $\Delta_{conf}S$ of three stable $[C_3mim]^+$ conformers (Fig. 1) and the anions' configurational entropy ($\Delta_{config}S$). When $[C_3mim]_2[MnClBr_3]$ was cooled, crystallization (T_{C1}) was observed. Furthermore, T_{C2} and T_m were determined after heating. The degrees of cation – anion coupling could differ between $[C_3mim]_2[MnCl_3Br]$ and $[C_3mim]_2[MnClBr_3]$. As previously stated (Fig. 4), $[C_3mim]_2[MnBr_4]$ is segregated based on irreversible crystal polymorphs. T_m of a series of $[C_3mim]_2[MnCl_{4-m}Br_m]$ was also affected by anions' $\Delta_{config}S$. Because of the largest $\Delta_{config}S$, $[C_3mim]_2[MnCl_2Br_2]$ had the lowest T_m.

$[C_4mim]^+$ has four stable conformers (Fig. 1) [33]. A previous study [52] discovered that grass transition or crystallization in $[C_4mim][X]$ was dependent on the $[X]^-$ type of anion. Since Cl^-, Br^-, I^-, $[BF_4]^-$ and $[PF_6]^-$ have no contribution to conformational entropy, crystallizations in $[C_4mim][X]$ with symmetric anions were alternated. However, a glass transition occurred in $[C_4mim]_2[MnCl_4]$ with a symmetric anion (Fig. 7). We conclude that the kinetic effect of $[MnBr_4]^{2-}$ was not in-

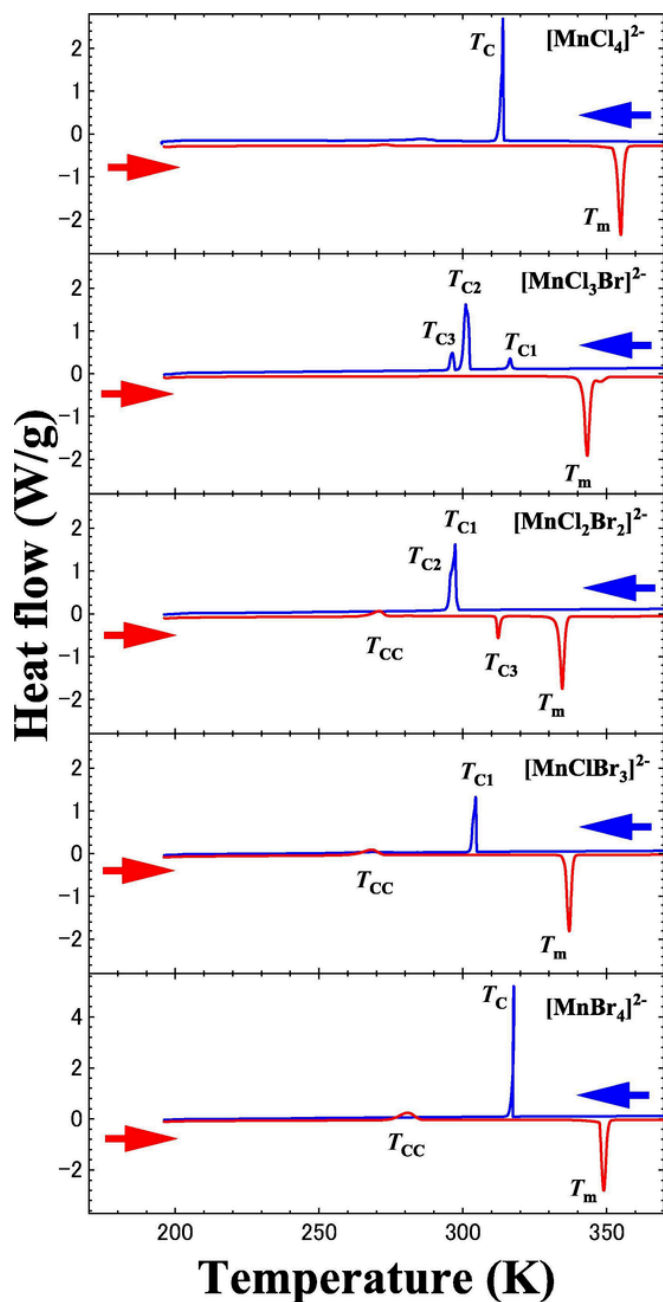**Fig. 5.** DSC thermal traces of $[C_2mim]_2[MnCl_{4-m}Br_m]$.

Fig. 6. DSC thermal traces of $[C_3mim]_2[MnCl_{4-m}Br_m]$.

significant in the unit cell, and $\Delta_{fus}S$ in Eq. (2) increased. Furthermore, the glass transition was indicated by $[C_4mim]_2[MnCl_{4-m}Br_m]$ ($m = 1, 2,$ and 3) with asymmetric anions. Consequently, crystallization or cold crystallization was suppressed below $m = 3$. Cold crystallization was observed only after heating $[C_4mim]_2[MnBr_4]$ (Fig. 7). It could be aided by the relatively small $\Delta_{kin}S$ of $[MnCl_4]^{2-}$. The various frequency behaviors of symmetric anions in $[C_4mim]_2[MnCl_4]$ and $[C_4mim]_2[MnBr_4]$ reflect the different contributions of $\Delta_{kin}S$, which are derived from the mass effect of the anions.

3.5. Magnetic properties of mILs

SQUID determined the magnetic properties of mILs between 2 and 300 K. The temperature dependence of the inverse magnetic suscepti-bility (χ_m^{-1}) of $[C_2mim]_2[MnCl_{4-m}Br_m]$ ($m = 0, 1, 2, 3,$ and 4) is shown in Fig. 8. Here, χ_m is the field-cooled molar susceptibility, and χ_m^{-1} is
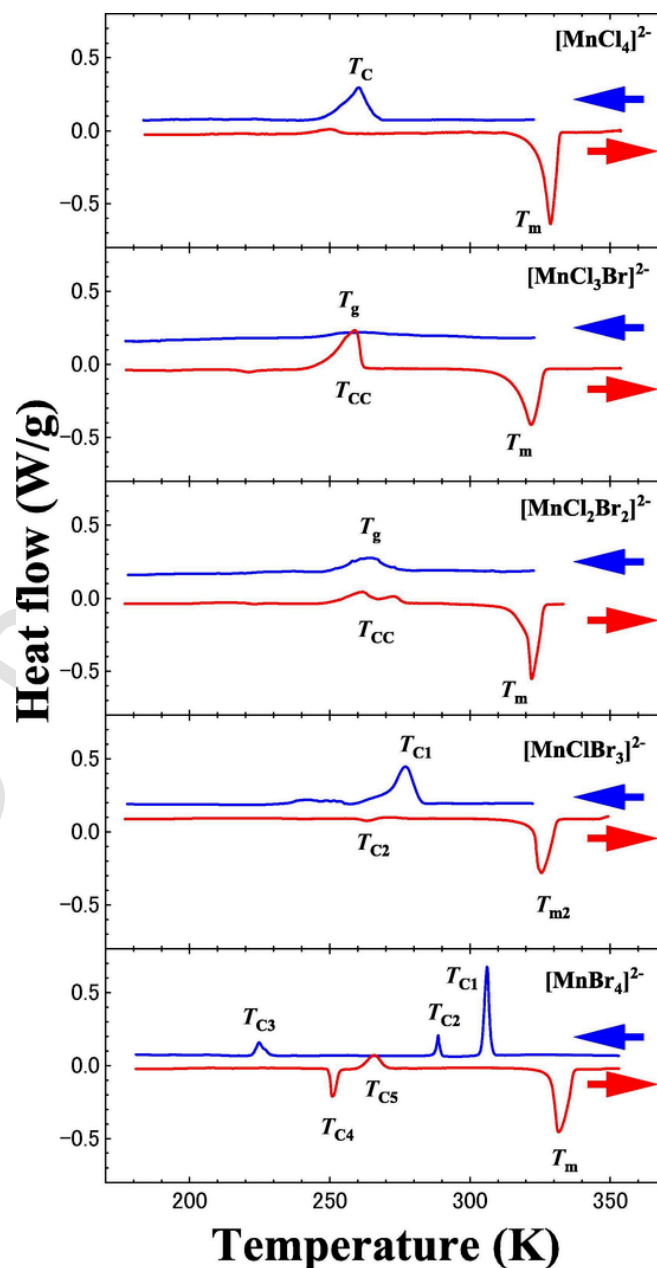
the zero-field-cooled one. For $[C_2mim]_2[MnCl_{4-m}Br_m]$ ($m = 0, 1, 2, 3,$ and 4), the Currie – Weiss law follows a linear relationship on the tem-perature scale in the χ_m^{-1}–T plot (Fig. 8). A slight asymmetric anion ef-fect of the anions indicated the paramagnetic property of all mILs. For example, the effective paramagnetic moment (μ_{eff}) of $[C_2mim]_2[MnCl_4]$ was calculated to be 5.40 μ_B, which is comparable to S = 5/2 spin's 5.92 μ_B. The μ_{eff} values of $[C_2mim]_2[MnCl_{4-m}Br_m]$ increased as m in-creased. The μ_{eff} values are m-dependent, suggesting that the Br substi-tution to the anions contributed to the intramolecular distances of the anions rather than the μ_{eff} values. The paramagnetic behavior could not conflict with the orientational disorders of the tetrahedral anions (Fig. S3). Even large unit cells with the orientational disorder could not in-duce long-range ferro or antiferro magnetic orders.

The magnetic properties of the $[FeCl_4]^-$-base system were drasti-cally altered by the alkyl chain length of $[C_nmim]^+$. For example, $[C_2mim][FeCl_4]$ [27] and $[C_4mim][FeCl_4]$ [20] showed antiferromag-netic and paramagnetic behavior, respectively. $[C_nmim]_2[MnBr_4]$
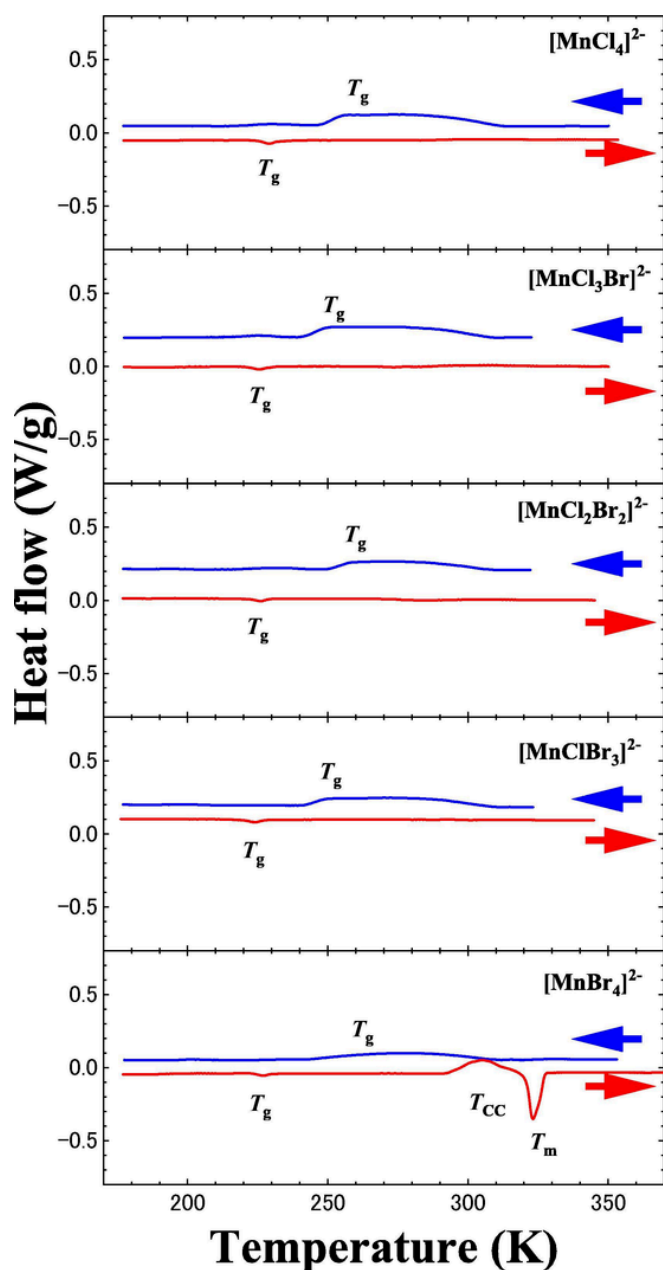
Fig. 7. DSC thermal traces of [C$_4$mim]$_2$[MnCl$_{4-m}$Br$_m$].

Fig. 8. Temperature dependency of χ_m^{-1} for [C$_2$mim]$_2$[MnCl$_{4-m}$Br$_m$] under 100 Oe.

tetrahedral anions in the unit cells resulted in a lack of magnetic long-range order.

CRediT authorship contribution statement

Hiroshi Abe : Conceptualization, Writing – original draft, Writing – review & editing. **Shin Kobayashi :** Data curation. **Kohei Ogawa :** Data curation. **Kanta Imai :** Data curation. **Kaito Koshiji :** Data curation. **Miku Hoshino :** Data curation. **Takaaki Hirano :** Data curation. **Yoshiaki Hata :** Data curation, Formal analysis. **Hiroaki Kishimura :** Data curation, Formal analysis. **Mikio Uruichi :** Data curation.

Declaration of Competing Interest

The authors declare that they have no known competing financial interests or personal relationships that could have appeared to influence the work reported in this paper.

Data availability

Data will be made available on request.

Acknowledgments

Appendix A. Supplementary material

Supplementary data to this article can be found online at https://doi.org/10.1016/j.chemphys.2023.111872.

References

[1] T. Welton, Room-temperature ionic liquids. solvents for synthesis and catalysis, Chem. Rev. 99 (1999) 2071–2083.
[2] H. Tokuda, S. Tsuzuki, M.A.B.H. Susan, K. Hayamizu, M. Watanabe, How ionic

---

(n = 2, 3 and 4) contrastingly belonged to the same paramagnetic property as shown in Fig. S5. The μ_{eff} values decreased proportionally to the length of the alkyl chain. Consequently, long-range magnetic order did not emerge in [C$_n$mim]$_2$[MnCl$_{4-m}$Br$_m$].

4. Conclusion

The simultaneous XRD and DSC measurements were used to determine the low-temperature phase behaviors of [C$_n$mim]$_2$[MnCl$_{4-m}$Br$_m$] (n = 2, 3, and 4; m = 0, 1, 2, 3, and 4). At low temperatures, complicated and irreversible crystal polymorphs appeared in [C$_3$mim][MnBr$_4$] with a symmetric anion. In the melting points of the mILs, conformational and configurational entropy effects were observed. Glass transition, crystallization, cold crystallization, and melting point were all governed by cation conformers and asymmetric anions. The Mn-based anions have a paramagnetic property. The orientational disorders of
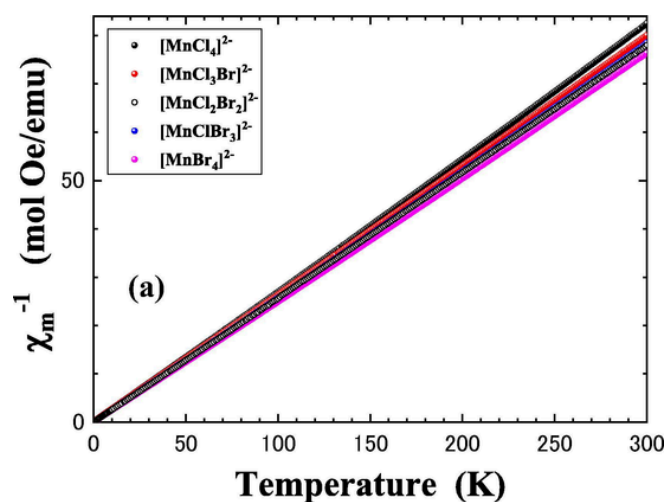
are room-temperature ionic liquids? an indicator of the physicochemical properties, J. Phys. Chem. B 110 (2006) 19593–19600.

[3] J.F. Wishart, E.W. Castner Jr, The physical chemistry of ionic liquids, J. Phys. Chem. B 111 (2007) 4639–4640.

[4] H.-Y. Han, X. Geng, B.-X. Zhang, J. Meng, X. Liu, X.-M. He, Z.-G. Liu, Y.-F. Gao, D. Liu, X.-M. Hu, Synthesis of novel functional ionic liquids and their application in biomass, RSC Adv. 9 (2019) 29652–29658.

[5] S.K. Singh, A.W. Savoy, Ionic liquids synthesis and applications: an overview, J. Mol. Liq. 297 (2020) 112038–1112023.

[6] Y. Yoshida, H. Kitagawa, Chromic ionic liquids, ACS Appl. Electron. Mater. 3 (2021) 2468–2482.

[7] S. Koutsoukos, J. Becker, A. Dobre, Z. Fan, F. Othman, F. Philippi, G.J. Smith, T. Welton, Synthesis of aprotic ionic liquids, Nat. Rev. Methods Prime. 2 (2022).

[8] N.V. Plechkova, K.R. Seddon, Applications of ionic liquids in the chemical industry, Chem. Soc. Rev. 37 (2008) 123–150.

[9] P. Berton, N. Abidi, J.L. Shamshina, Ionic liquids: implementing objectives of sustainability for the next generation chemical processes and industrial applications, Curr. Opin. Green Sust. Chem. 35 (2022) 100625–100627.

[10] A.J. Greer, J. Jacquemin, C. Hardacre, Industrial applications of ionic liquids, Molecules 25 (2020) 5207–5231.

[11] D.R. MacFarlane, N. Tachikawa, J.M. Maria Forsyth, P.C. Pringle, G.D. Howlett, J.H.D. Elliott, Jr., M. Watanabe, P. Simon, C.A. Angell, Energy applications of ionic liquids, Energy Environ. Sci. 7 (2014) 232–250.

[12] M. Watanabe, M.L. Thomas, S. Zhang, K. Ueno, T. Yasuda, K. Dokko, Application of ionic liquids to energy storage and conversion materials and devices, Chem. Rev. 117 (2017) 7190–7239.

[13] T. Welton, Ionic liquids in catalysis, Coord. Chem. Rev. 248 (2004) 2459–2477.

[14] S. Zeng, X. Zhang, L. Bai, X. Zhang, H. Wang, J. Wang, D. Bao, M. Li, X. Liu, S. Zhang, Ionic-liquid-based CO_2 capture systems: structure, interaction and process, Chem. Rev. 117 (2017) 9625–9673.

[15] A. Pinkert, K.N. Marsh, S. Pang, M.P. Staiger, Ionic liquids and their interaction with cellulose, Chem. Rev. 109 (2009) 6712–6728.

[16] V. Venkatraman, S. Evjen, H.K. Knuutila, A. Fiksdahl, B.K. Alsberg, Predicting ionic liquid melting points using machine learning, J. Mol. Liq. 264 (2018) 318–326.

[17] K. Paduszyński, K. Kłębowski, M. Królikowska, Predicting melting point of ionic liquids using QSPR approach: literature review and new models, J. Mol. Liq. 344 (2021) 117631–1117619.

[18] S. Koutsoukos, F. Philippi, F. Malaret, T. Welton, A review on machine learning algorithms for the ionic liquid chemical space, Chem. Sci. 12 (2021) 6820–6843.

[19] T. Endo, K. Sunada, H. Sumida, Y. Kimura, Origin of low melting point of ionic liquids: dominant role of entropy, Chem. Sci. 13 (2022) 7560–7565.

[20] S. Hayashi, H. Hamaguchi, Discovery of a Magnetic Ionic Liquid [bmim]FeCl₄, Chem. Lett. 34 (2004) 1590–1591.

[21] J.-G. Li, Y.-F. Hu, S.-F. Sun, S. Ling, J.-Z. Zhang, Ionic structures of nanobased FeCl₃/[C₄mim]Cl ionic liquids, J. Phys. Chem. B 116 (2012) 6461–6464.

[22] J. Wang, H. Yao, Y. Nie, X. Zhang, J. Li, Synthesis and characterization of the iron-containing magnetic ionic liquids, J. Mol. Liq. 169 (2012) 152–155.

[23] C. Zhou, X. Yu, H. Ma, X. Huang, H. Zhang, J. Jin, Properties and catalytic activity of magnetic and acidic ionic liquids: experimental and molecular simulation, Carbohydr. Polym. 105 (2014) 300–307.

[24] Y. Kemmizaki, H. Tsutsumi, K. Ueno, Redox active Glyme-Li salt solvate ionic liquids based on tetrabromoferrate(III), Electrochem. 86 (2018) 46–51.

[25] M.S. Sitze, E.R. Schreiter, E.V. Patterson, R.G. Freeman, Ionic liquids based on FeCl3 and FeCl2. Raman scattering and ab initio calculations, Inorg. Chem. 40 (2001) 2298–2304.

[26] H. Li, W. Zhu, Y. Chang, W. Jiang, M. Zhang, S. Yin, J. Xia, H. Li, Theoretical investigation of the interaction between aromatic sulfur compounds and [BMIM]⁺[FeCl₄]⁻ ionic liquid in desulfurization: anovel charge transfer mechanism, J. Mol. Graphics Model. 59 (2015) 40–49.

[27] I. dePedro, D.P. Rojas, J.A. Blanco, J. Rodríguez Fernández, Antiferromagnetic ordering in magnetic ionic liquid Emim[FeCl₄], J. Mag. Mag. Mater. 323 (2011) 1254–1257.

[28] T. Backer, O. Breunig, M. Valldor, K. Merz, V. Vasylyeva, A.-V. Mudring, In-situ crystal growth and properties of the magnetic ionic liquid [C₂mim][FeCl₄], Cryst. Growth Des. 11 (2011) 2564–2571.

[29] A. García-Saiz, I. de Pedro, L. Fernández Barquín, M.T. Fernández-Díaz, J. A. Blanco, J. Rodríguez Fernández, Neutron Powder Diffraction study of the Magnetic Ionic Liquid Emim[FeCL₄] and its deuterated phase, J. Phys.: Conf. Ser. 663 (2015) 012008-5.

[30] A. García-Saiz, I. de Pedro, J.A. Blanco, J. González, J.R. Fernández, Pressure effects on Emim[FeCl₄], a magnetic ionic liquid with three-dimensional magnetic

[31] A. García-Saiz, I. de Pedro, P. Migowski, O. Vallcorba, J. Junquera, J.A. Blanco, O. Fabelo, D. Sheptyakov, J.C. Waerenborgh, M.T. Fernández-Díaz, J. Rius, J. Dupont, J.A. Gonzalez, J.R. Fernández, Anion−π and halide−halide nonbonding interactions in a new ionic liquid based on imidazolium cation with three-dimensional magnetic ordering in the solid state, Inorg. Chem. 53 (2014) 8384–8396.

[32] H. Abe, S. Maruyama, Y. Hata, S. Shimono, H. Kishimura, Asymmetric effects of anions in magnetic ionic liquids, Chem. Phys. Lett. 748 (2020) 137389−5.

[33] T. Endo, T. Higuchi, Y. Kimura, DFT study on conformation of 1-alkyl-3-methylimidazolium with ethyl, propyl, butyl, pentyl, and hexyl group, Bull. Chem. Soc. Jpn. 93 (2020) 720–729.

[34] Y. Koyama, S. Shimono, H. Kishimura, T. Takekiyo, Y. Yoshimura, H. Abe, K. Matsuishi, High-pressure crystal polymorphs in 1-butyl-3-methylimidazolium perfluorobutanesulfonate, J. Mol. Liq. 335 (2021) 116415–116417.

[35] T. Runka, M. Berkowski, Perovskite La₁₋ₓSrₓGa₁₋yMnyO₃ solid solution crystals: Raman spectroscopy characterization, J. Mater. Sci. 47 (2012) 5393–5401.

[36] V. Favre-Nicolin, R. Cerny, FOX, 'free objects for crystallography': a modular approach to ab initio structure determination from powder diffraction, J. Appl. Cryst. 35 (2002) 734–743.

[37] R. Oishi-Tomiyasu, Robust powder auto-indexing using many peaks, J. Appl. Cryst. 47 (2014) 593–598.

[38] A.A. Granovsky, Firefly version 8, < http://classic.chem.msu.su/gran/firefly/index.html >.

[39] M.W. Schmidt, K.K. Baldridge, J.A. Boatz, S.T. Elbert, M.S. Gordon, J.H. Jensen, S. Koseki, N. Matsunaga, K.A. Nguyen, S. Su, T.L. Windus, M. Dupuis, J.A. Montgomery, General atomic and molecular electronic structure system, J. Comput. Chem. 14 (1993) 1347–1363.

[40] N.A. Wojcik, D.A. Kowalska, M. Trzebiatowska, E. Jach, A. Ostrowski, W. Bednarski, M. Gusowski, P. Staniorowski, A. Cizman, Tunable dielectric switching of (quinuclidinium)[MnCl₄] hybrid compounds, J. Phys. Chem. C 125 (2021) 16810–16818.

[41] H. Abe, M. Aono, T. Takekiyo, Y. Yoshimura, A. Shimizu, Phase behavior of water-mediated protic ionic liquid: ethylammonium nitrate, J. Mol. Liq. 241 (2017) 301–307.

[42] H. Abe, T. Takekiyo, Y. Yoshimura, A. Shimizu, S. Ozawa, Multiple crystal pathways and crystal polymorphs in protic ionic liquids, J. Mol. Liq. 269 (2018) 733–737.

[43] H. Abe, H. Kishimura, T. Takekiyo, T. Hanasaki, Y. Yoshimura, N. Hamaya, Low-temperature and high-pressure phase changes of room temperature ionic liquids, J. Mol. Liq. 300 (2020) 112340–112349.

[44] Y. Koyama, S. Shimono, H. Abe, K. Matsuishi, Crystal polymorphs in 1-alkyl-3-methylimidazolium perfluorobutanesulfonate ionic liquids, J. Mol. Liq. 317 (2020) 113908–7.

[45] H. Abe, H. Kishimura, Multistep phase transition in 1-decyl-3-methylimidazolium nitrate ionic liquid, J. Mol. Liq. 352 (2022) 118695–118698.

[46] H. Abe, H. Kishimura, M. Uruichi, A phase variety of fluorinated ionic liquids: Molecular conformational and crystal polymorph, Spectrochim. Acta A 286 (2023) 121948–7.

[47] M. Shigemi, T. Takekiyo, H. Abe, Y. Yoshimura, Pressure-induced crystallization of 1-butyl-3-methylimidazolium hexafluorophosphate, High Press. Res. 33 (2013) 229–233.

[48] H. Abe, N. Hamaya, Y. Koyama, H. Kishimura, T. Takekiyo, Y. Yoshimura, D. Wakabayashi, N. Funamori, K. Matsuishi, Long periodic structure of a room-temperature ionic liquid by high-pressure small-angle X-Ray scattering and wide-angle X-Ray scattering: 1-decyl-3-methylimidazolium chloride, ChemPhysChem 19 (2018) 1441–1447.

[49] H. Abe, T. Takekiyo, Y. Yoshimura, N. Hamaya, S. Ozawa, Crystal polymorphs and multiple crystallization pathways of highly pressurized 1-ethyl-3-methylimidazolium nitrate, Aust. J. Chem. 72 (2019) 87–92.

[50] H. Abe, Y. Koyama, H. Kishimura, K. Matsuishi, High-pressure crystal polymorph of the protic ionic liquid: Ethylammonium nitrate, J. Mol. Liq. 318 (2020) 113959–6.

[51] H. Abe, Y. Koyama, S. Shimono, H. Kishimura, K. Matsuishi, High-pressure crystal polymorphs and multiple pathways in 1-hexyl-3-methylimidazolium perfluorobutanesulfonate ionic liquid, Chem. Phys. 557 (2022) 111479–7.

[52] H. Abe, S. Tsuzuki, S. Ozawa, Anion effects on amorphization and crystallization in room-temperature ionic liquids, Chem. Phys. Lett. 712 (2018) 30–33.

[53] K. Momma, F. Izumi, VESTA 3 for three-dimensional visualization of crystal, volumetric and morphology data, J. Appl. Cryst. 44 (2011) 1272–1276.